nature COMMUNICATIONS

ARTICLE

Received 7 Jun 2012 | Accepted 8 Feb 2013 | Published 12 Mar 2013

DOI: 10.1038/ncomms2584

Large spin-orbit coupling in carbon nanotubes

G.A. Steele[1], F. Pei[1], E.A. Laird[1], J.M. Jol[1], H.B. Meerwaldt[1] & L.P. Kouwenhoven[1]

It has recently been recognised that the strong spin-orbit interaction present in solids can lead to new phenomena, such as materials with non-trivial topological order. Although the atomic spin-orbit coupling in carbon is weak, the spin-orbit coupling in carbon nanotubes can be significant due to their curved surface. Previous works have reported spin-orbit couplings in reasonable agreement with theory, and this coupling strength has formed the basis of a large number of theoretical proposals. Here we report a spin-orbit coupling in three carbon nanotube devices that is an order of magnitude larger than previously measured. We find a zero-field spin splitting of up to 3.4 meV, corresponding to a built-in effective magnetic field of 29 T aligned along the nanotube axis. Although the origin of the large spin-orbit coupling is not explained by existing theories, its strength is promising for applications of the spin-orbit interaction in carbon nanotubes devices.

[1] Kavli Institute of NanoScience, Delft University of Technology, PO Box 5046, Delft 2600GA, The Netherlands. Correspondence and requests for materials should be addressed to G.A.S. (email: g.a.steele@tudelft.nl).

In solids, spin-orbit coupling has recently become a very active topic, in particular in the context of its role in a new class of materials with a non-trivial topological order[1–3], and its use to enable new control techniques in solid-state qubits based on manipulating spins with electric fields[4,5]. Owing to the low atomic number of the carbon nucleus, the spin-orbit interaction in carbon materials is, in general, weak. An example of this is flat graphene, in which intrinsic spin-orbit effects are expected to appear at energy scales of only 1 μeV (10 mK)[6,7]. In carbon nanotubes, however, the curvature of the surface breaks a symmetry that is present in graphene. This broken symmetry enhances the intrinsic spin-orbit coupling in carbon nanotubes compared with flat graphene, with theoretical estimates predicting splittings on the order of 100 μeV, an energy scale easily accessible in transport measurements at dilution refrigerator temperatures, and recently observed in experiments[8–11]. Experiments so far have reported spin-orbit splittings typically in the range of hundreds of μeV, and which were reasonably consistent with theoretical predictions.

Since it was first observed experimentally, the spin-orbit interaction in carbon nanotubes has attracted significant theoretical attention, and has been the basis of a large number of theoretical proposals. Recent calculations predict that it enables fast electrical spin manipulation in carbon nanotube spin qubits[12,13], that it can couple to the phase of Josephson supercurrents through Andreev bound states in nanotube superconducting junctions[14,15], that it allows the spin to couple to the high quality vibrational modes of nanotubes[16,17] and that it could be interesting for the study of topological liquids and Majorana bound states[18–22]. These many exciting proposed applications could potentially benefit from a stronger spin-orbit coupling.

Here, we present measurements of three carbon nanotube devices which have spin-orbit couplings an order of magnitude larger than that predicted by theory. We observe the spin-orbit coupling by measuring the magnetic field dependence of the ground states of clean carbon nanotube quantum dots in the few-electron and few-hole regime[23]. We use a Dirac-point crossing at a low magnetic field as a tool for distinguishing orbital-type coupling[24,25,6] from the recently predicted Zeeman-type coupling[26–28]. Although it is not understood why the spin-orbit coupling we observe is so much larger than that predicted by tight-binding calculations, its large magnitude is attractive for implementing the theoretical proposals for using the carbon nanotube spin-orbit coupling for a wide range of new experiments.

Results

Spin-orbit coupling in a few electron nanotube quantum dot. The devices are made using a fabrication technique in which the nanotube is deposited in the last step of the fabrication. Figure 1a shows a schematic of a single quantum dot device with three gates. Figure 1b shows a scanning electron microscope image of device 1, taken after all measurements were completed. Similar to previous reports[23], we are able to tune the device to contain only a single electron (see Supplementary Note 1 and Supplementary Figs S1,S2). An external magnetic field is applied in-plane, perpendicular to the trench. As we do not control the direction of the growth process, this magnetic field often has a misalignment to the nanotube, but still contains a large component parallel to the nanotube axis. All measurements were performed in a dilution refrigerator with an electron temperature of 100 mK.

In Fig. 1c–f, we show the magnetic field dependence of the Coulomb peaks of the first four electrons in a carbon nanotube quantum dot in device 1. In the few electron regime, we estimate the single-particle level spacing of the quantum dot to be $\Delta E_{SP} = 11$ meV (see Supplementary Fig. S3). Note that similar to recent reports[29], this device exhibits a crossing of the Dirac point at an anomalously low magnetic field, causing a reversal of the orbital magnetic moment of one of the valleys at $B_{\mathrm{Dirac}} = 2.2$ T (see Fig. 2c–f). The low B_{Dirac} indicates a small shift of the $k_\perp$

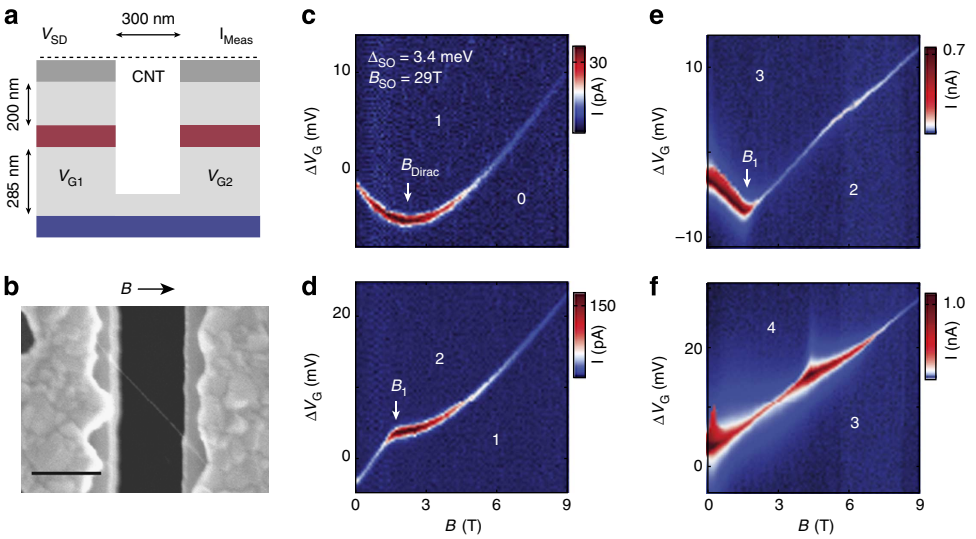

Figure 1 | A 29 T spin-orbit magnetic field in a carbon nanotube. (**a**) A schematic of device 1. (**b**) A scanning electron microscope (SEM) image of device 1. Scale bar, 300 nm. Scale bar, 300 nm. The arrow indicates the direction of the applied magnetic field *B*. (**c–f**) Magnetic field dependence of the Coulomb peak positions of the first four electrons in the device. $V_{SD} = 200$ μV in (**c**,**d**) and $V_{SD} = 150$ μV in (**e**,**f**). ΔV_G corresponds to a small offset in gate voltage used to track the Coulomb peaks as a function of magnetic field. The crossing of the Dirac point reverses the sign of the orbital magnetic moment of the lower energy valley at a field $B_{\mathrm{Dirac}} = 2.2$ T. Without spin-orbit coupling, the first two electrons would both occupy the valley with the decreasing orbital energy, and would result in a downwards slope in both (**c**,**d**) at fields below B_{Dirac}. Here, the second electron, (**d**), instead occupies a valley with increasing orbital energy, a unique signature of the nanotube spin-orbit coupling, up to a field $B_1 = 1.6$ T. From the ground state energies extracted from the Coulomb peak positions, Fig. 3 (**a**), we obtain a spin-orbit splitting $\Delta_{SO} = 3.4 \pm 0.3$ meV, corresponding to a built-in spin-orbit magnetic field $B_{SO} = 29$ T seen by the electron spin. The sharp kinks at B_1 in (**d**,**e**) imply weak valley mixing: we estimate $\Delta_{KK'} \sim 0.1$ meV.

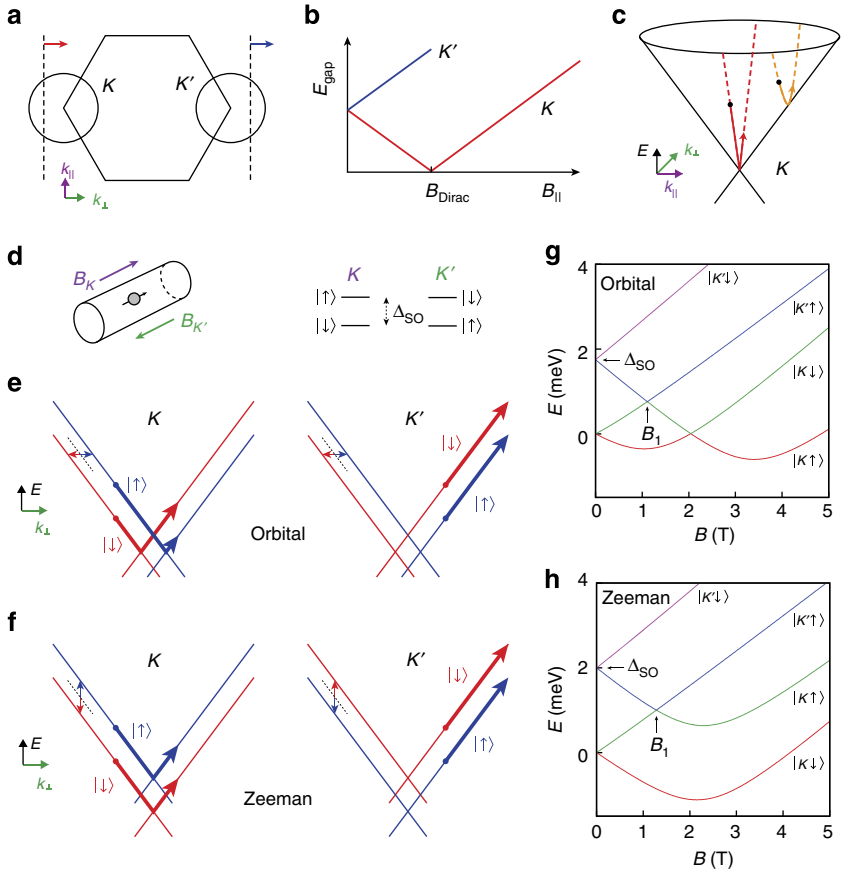

Figure 2 | Spin-orbit coupled states in a nearly-metallic nanotube. (**a**) The two nanotube valleys (*K* and *K*′) arise from the intersection of the $k_\perp$ quantisation lines (dashed) with the Dirac cones of the graphene bandstructure. A magnetic field applied parallel to the nanotube axis shifts both quantisation lines horizontally, reducing the bandgap in one *K* point and increasing it for the other, illustrated in (**b**). At a sufficiently large magnetic field B_{Dirac}, one valley (red line) crosses the Dirac point, after which the orbital magnetic moment changes sign. (**c**) With $k_\parallel = 0$, the lowest energy state in the conduction band would follow a v-shape with a sharp kink at B_{Dirac} (red line in **b**,**c**). A finite $k_\parallel$ from confinement in the axial direction results instead in a hyperbolic shape (orange line in **c**). (**d**) The spin-orbit interaction in the nanotube results in an internal magnetic field aligned along the nanotube axis whose direction depends on the valley the electron occupies. (**e**) In the orbital-type spin-orbit coupling[24,25,6], this magnetic field results in a spin-dependent shift of $k_\perp$, while the Zeeman-type coupling, (**f**), gives a valley dependent vertical shift in energy[26–28]. (**g**,**h**) Calculated energy spectrum of the first shell for a purely orbital-type coupling, (**g**), and a purely Zeeman-type coupling, (**h**), with parameters chosen to illustrate the difference between the two types of spectra. Colours indicate the ground state energies of the four electrons that would fill the shell. In (**g**), electrons experience a spin-dependent $k_\perp$ shift, resulting in two separate Dirac crossings[10], an effect absent in (**h**).

quantisation line from the Dirac point (Fig. 2a), and would predict a small electronic bandgap contribution from the momentum $k_\perp$ of the electronic states around the nanotube circumference: $E_{gap}^{k_\perp} = 2\hbar v_F k_\perp = 7$ meV. We describe a nanotube with a low Dirac-field crossing as 'nearly metallic', as the $k_\perp$ quantisation line nearly passes through the Dirac point. The bandgap in our device does not vanish at B_{Dirac}, as would be expected, but instead retains a large residual contribution $E_{gap}^{residual} = 80$ meV, similar to previous reports[29]. It has been suggested that this residual energy gap could arise from a Mott-insulating state, although its exact origin remains a topic of investigation that we will not address here. This low Dirac-field crossing does not affect the spin-orbit spectra we observe, and will later provide a unique signature for distinguishing orbital[24,25,6] from Zeeman-[26–28] type coupling. We first focus on the behaviour at magnetic fields below B_{Dirac}.

The unambiguous signature of the nanotube spin-orbit interaction can be seen by comparing the low magnetic field behaviour in Fig. 1c,d. Owing to the opposite direction of circulation of the electronic states about the nanotube circumference, the bandgap of the *K* and *K*′ valleys both change in the presence of a parallel magnetic field[30,31]. The bandgap in one valley increases and the other decreases, both with a rate given by $dE/dB = 2\mu_{orb}$, where $\mu_{orb} = dev_{F\perp}/4$ ($\mu_{orb} \sim 220\,\mu$eV/T for $d = 1$ nm). In the absence of spin-orbit coupling, the first two electrons would both occupy the valley with lower energy, and thus the first two ground states would both shift down in energy with magnetic field. In Fig. 1c,d, we observe a different behaviour: in particular, at low magnetic fields, the second electron instead occupies the valley that is increasing in energy with magnetic field. The occupation of the 'wrong valley' by the second electron is a result of the nanotube spin-orbit interaction[8]: the spin-orbit coupling in nanotubes results in an effective magnetic field aligned along the nanotube axis, which points in opposite directions for the *K* and *K*′ valleys (Fig. 2d). This magnetic field produces a spin splitting Δ_{SO} for the two spin species in the same valley. In an external magnetic field, the second electron then enters the 'wrong' valley, and persists there until the energy penalty for this exceeds Δ_{SO}. In device 1, from the extract ground-state spectra shown in Fig. 3(a), we find a $\Delta_{SO} = 3.4 \pm 0.3$ meV. In addition to the ground state measurements, states consistent with such a splitting have been observed in finite bias excited state

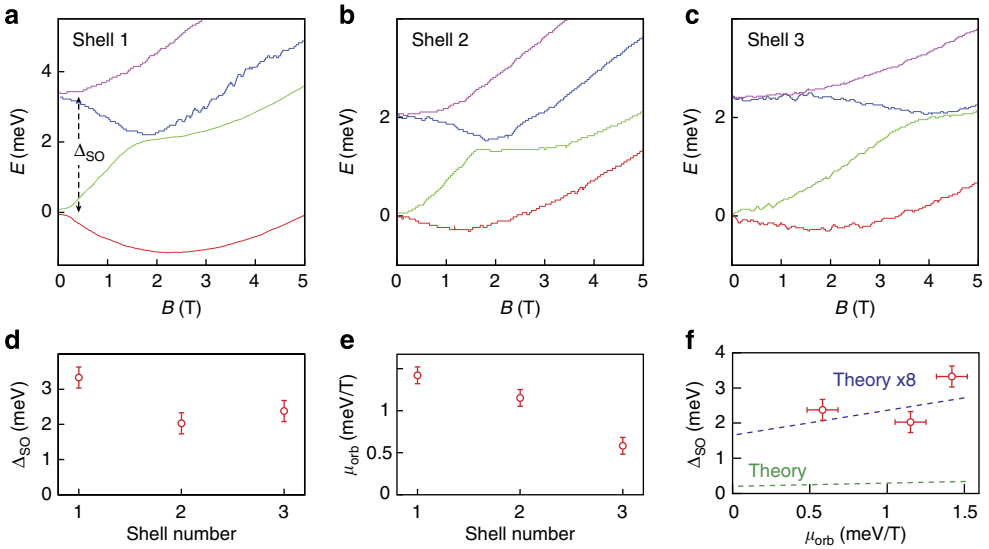

Figure 3 | Spin-orbit coupling in the first three electronic shells. (**a**–**c**) Observed energy spectra of the first 12 electrons in device 1. The spectra exhibits a four-fold shell filling, with the spin-orbit electronic spectrum visible in all three shells. Extracted Δ_{SO} are shown in (**d**). Comparing with the spectra for the two types of nanotube spin-orbit coupling (Fig. 2g,h), it is clear the device exhibits a Zeeman-type coupling. Deviations from the model are discussed in the main text. (**e**) μ_{orb} as a function of the shell number. For larger shells, electrons are confined in an electronic level with a larger value of $k_{\parallel}$. The correspondingly larger momentum along the nanotube axis decreases the velocity around the nanotube circumference, reducing the orbital magnetic moment[11,32]. (**f**) Δ_{SO} as a function of μ_{orb}. The green dashed line shows the maximum spin-orbit coupling expected from theory with α and β for a 3-nm nanotube (equation 1 together with the scaling of α with the magnetic moment). By scaling coefficients α and β by a factor of 8 (blue line), we can reproduce the order of magnitude of the spin-orbit coupling in our device.

spectroscopy (see Supplementary Figs S3,S4). We have also observed a large $\Delta_{SO} = 1.5 \pm 0.2$ meV in a second similar single-dot device (see Supplementary Figs S5–S9, and Supplementary Note 2).

Spin-orbit coupling in nearly-metallic carbon nanotubes. In Fig. 2, we show calculated energy levels of a nearly-metallic carbon nanotube including the spin-orbit interaction. In carbon nanotubes, there are two contributions to the spin-orbit coupling, one which we describe as orbital-type coupling, which induces a shift in the $k_{\perp}$ quantisation line[26,27,28] and results in an energy shift proportional to the orbital magnetic moment. The second type, which we describe as Zeeman type, shifts only the energy of the electron spin with no shift in $k_{\perp}$. The energy and momentum shifts from these couplings are illustrated in Fig. 2e,f. Combining these two effects, we have the following Hamiltonian for the spin-orbit interaction (equation 71 in ref. 28):

$$H_{SO}^{cv} = \alpha S^z \sigma_1 + \tau \beta S^z \qquad (1)$$

where S^Z is the spin component along the axis of the nanotube, σ_1 leads to a spin-dependent horizontal shift of the dispersion relation along $k_{\perp}$ that is of opposite sign in different valleys, while τ leads to a spin-dependent vertical shift that is opposite in the two valleys. The first term represents the orbital-type of coupling, while the second represents the Zeeman-type coupling. The coefficients α and β determine the strength of the two types of coupling, with $\Delta_{SO}^{orb} = \alpha = (-0.08\,\text{meV nm})/r$ at $k_{\parallel} = 0$, and $\Delta_{SO}^{Zeeman} = \beta = (-0.31 \cos 3\theta\,\text{meV nm})/r$ where θ is the chiral angle of the nanotube wrapping vector[28], and r is the radius of the nanotube in nanometres. Through the $\cos(3\theta)$ term, Δ_{SO}^{Zeeman} is dependent on the chirality of the nanotube, and is maximum for nanotubes with $\theta = 0$, corresponding to the zigzag wrapping vector. Direct experimental observation of the Zeeman-type coupling has been, until now, difficult. There have been two reported indications of a Zeeman-type coupling. The first is a different Δ_{SO} for holes and electrons[26,27], which is not present in the orbital-type spin-orbit models[24,25,6]. Such an asymmetry was observed in the initial experiments by Kuemmeth *et al.*[8], and motivated in part the initial theoretical work predicting the Zeeman-type coupling[26,27]. The second indication is a scaling of Δ_{SO} over a large number of electronic shells, as seen in recent experiments[11], from which a small Zeeman-type contribution was extracted.

The low Dirac-field crossing in the nearly-metallic carbon nanotubes studied here provides a unique signature that allows us to identify the type of coupling by looking at the energy spectrum of only a single shell. In Fig. 2g, we show the calculated energy spectrum for a nearly-metallic carbon nanotube with purely orbital-type coupling (see Supplementary Note 3 for details of the model). As the orbital-type coupling shifts $k_{\perp}$, the spin-up and spin-down states cross the Dirac point at significantly different magnetic fields[10]. For a purely Zeeman-type coupling, Fig. 2h, the two spin states cross the Dirac point at the same magnetic field. By comparing the theoretical predictions in Fig. 2g,h to the observed energy spectrum extracted from the Coulomb peaks in Fig. 3a, we can clearly identify a Zeeman-type spin-orbit coupling, suggesting that this nanotube has a chiral vector near $\theta = 0$. However, the magnitude of the spin-orbit splitting is much larger than that predicted by theory (see Supplementary Table S1 and Supplementary Note 4 for a summary of expected theoretical values and previous experimental observations). One possible origin for the observed discrepancy is an underestimate of the bare atomic spin-orbit coupling parameter from *ab-initio* calculations, which enters the tight-binding calculations as an empirical input parameter.

In Fig. 3, we show the ground state energies of the first 12 electrons as a function of magnetic field, extracted from the Coulomb peak positions (Supplementary Fig. S9). The ground states energies follow a four-fold periodic shell-filling pattern, with the spin-orbit split energy spectrum reproduced in the second and third electronic shell. In Fig. 3e, we plot the orbital

magnetic moment as a function of shell number, including a correction for the angle between the magnetic field and the nanotube axis. As reported previously[32], the orbital magnetic moment changes with shell number, an effect particularly strong in our device owing to the small $k_\perp$ implied by the low magnetic field Dirac crossing. In Fig. 3f, we plot the observed Δ_{SO} as a function of the orbital magnetic moment, together with the theoretical predictions from equation 1. In the plot, we have included the fact that the orbital coupling coefficient α in equation 1 scales with the orbital magnetic moment[11]. The green dashed line shows the prediction from equation 1 for a nanotube with a 3-nm diameter, emphasising the disagreement between measured and the theoretically predicted values. Also shown is the same prediction with the coefficients scaled by a factor of 8 in order to obtain the order of magnitude of the observed splitting.

Note that there are some discrepancies between the energy spectrum extracted from the Coulomb peak positions (Fig. 3a–c) and the theoretical spectra presented in Fig. 2. The first discrepancy is a small curvature of the extracted ground state energies at $B < 0.15$ T in Fig. 3a–c, which we attribute to artifacts from way in which the magnetic field sweeps were performed (see Supplementary Note 5 and Supplementary Fig. S10). The second discrepancy is a bending of the extracted energies at $B < 1.5$ T, particularly noticeable in the upper two states of the second and third shells (blue and purple lines in Fig. 3b,c), and a resulting suppressed slope for $B < 1.5$ T in these states. Correlated with the gate voltages and magnetic fields where the suppressed slopes occur, we observed a strong Kondo effect present in the odd valleys (see Supplementary Fig. S2). Owing to the strong tunnel coupling to the leads, the Kondo current in the valley can persist up to fields of 1.5 T (see Supplementary Fig. S9), and is stronger in the higher shells where the tunnel coupling to the leads is larger. The model described in Fig. 2 does not include higher-order effects, such as Kondo correlations, and it seems that it is no able to correctly predict the position of the Coulomb peak in these regions. Qualitatively, the magnetic moments associated with the states appear to be reduced by the strong Kondo effect, although the reason for this is not understood. Note that a suppressed magnetic moment will reduce the apparent spin-orbit splitting, and thus the large spin-orbit splittings reported here represent a lower bound.

Large spin-orbit coupling in a nanotube double quantum dot. In Fig. 4, we present data from a third device in a p–n double quantum dot configuration that also exhibits an unexpectedly large spin-orbit coupling (see Supplementary Note 6 and Supplementary Figs S11,S12 for device details and characterization). Figure 4c,d show measurements of the ground state energies of the first two electrons and first two holes in the device as a function of parallel magnetic field, measured by tracking the position of a fixed point on the bias triangle in gate space (coloured circles in Fig. 4a) as a function of magnetic field. The signature of the nanotube spin-orbit interaction can be clearly seen by the opposite slope of the first two electrons (holes) in Fig. 4c (Fig. 4d), and is consistent with the carbon nanotube spin-orbit spectrum far from the Dirac crossing, shown in Fig. 4b. The difference in the high magnetic field slopes corresponds to a

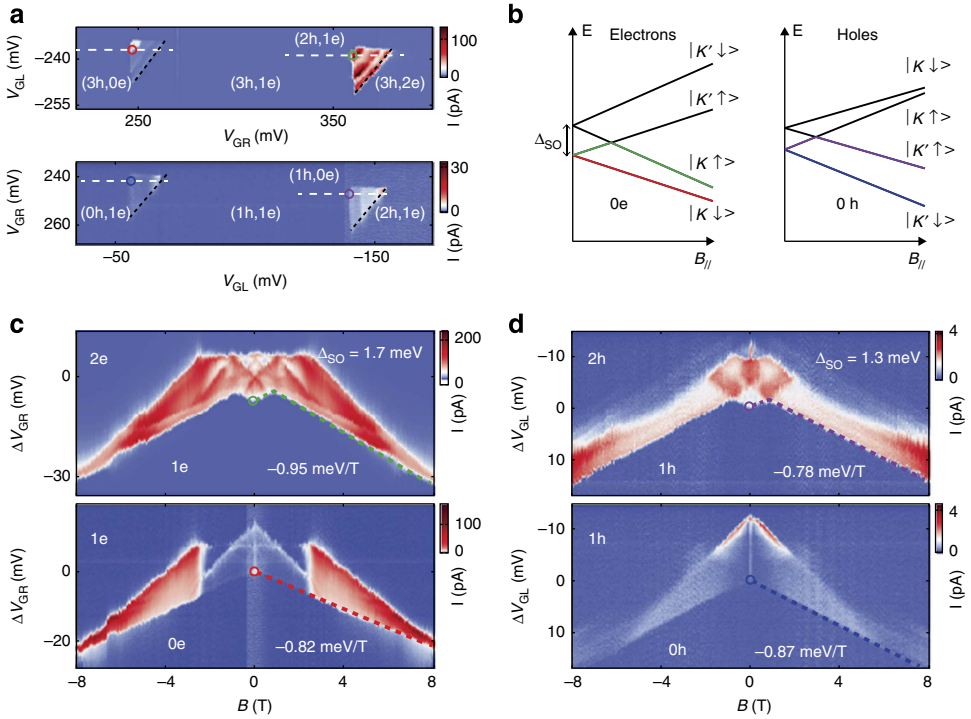

Figure 4 | Large spin-orbit coupling in a (p,n) double quantum dot. (**a**) Colour scale plots of the current at a source-drain bias $V_{sd} = 5$ mV and $B = 0$. Black dashed lines indicate the baseline of the triple-point bias triangles. Movement of the tip of the bias triangles (coloured circles) in gate space along line cuts in gate space (white dashed lines) with magnetic field is used in (**c**,**d**) to track the ground state energies. (**b**) Expected energy spectrum for the first shell of electrons and holes including the spin-orbit interaction. (**c**,**d**) Magnetic field dependence of line cuts in gate space (white dashed lines in **a**) for the first two electrons, (**c**), and holes, (**d**). Coloured circles indicate positions on the corresponding bias triangles in (**a**), and the dashed lines indicate the observed magnetic field dependence of the ground states, in good agreement with the spin-orbit spectrum, (**b**). High magnetic field slopes for the ground state energies are indicated in the figures. We extract spin-orbit splittings $\Delta_{SO}^{1e} = 1.7 \pm 0.1$ meV for the first electron shell and $\Delta_{SO}^{1h} = 1.3 \pm 0.1$ meV for the first hole shell. Excited states inside the bias triangles (colour scale data above dashed lines) exhibit a rich structure as a function magnetic field, which we discuss elsewhere[33].

Zeeman splitting with $g \sim 2$, as expected from the spin-orbit spectrum. By calibrating the gate voltage shifts into energy using the size and orientation of the finite bias triangles (see Supplementary Note 6), we extract an orbital magnetic moment of $\mu_{orb} = 0.8$ meV/T, a spin-orbit splitting $\Delta_{SO}^{1e} = 1.7 \pm 0.1$ meV for the first electron shell, and $\Delta_{SO}^{1h} = 1.3 \pm 0.1$ meV for the first hole shell. Estimating the diameter from the orbital magnetic moment, theory would predict a $\Delta_{SO}^{max} \sim 0.2$ meV for this device, an order of magnitude below the observed values. Note that device 3 exhibits a large spin-orbit coupling without a low B_{Dirac}, suggesting that these two phenomena are not linked.

From the slopes of the ground states, we predict that first two electron levels will cross at a magnetic field $B_2 = \Delta_{SO}/g\mu_B = 15$ T, while the first two hole levels do not cross. The crossing of the first two electron levels instead of the hole states, as was observed by Kuemmeth *et al.*[8], implies the opposite sign of the spin-orbit interaction, likely due to a different chirality of our nanotube. The absence of the low Dirac-field crossing, however, does not allow us to clearly separate the orbital and Zeeman contributions, as was possible for the other two devices.

Discussion

We have observed strong spin-orbit couplings in carbon nanotubes that are an order of magnitude larger than that predicted by theory, with splittings up to $\Delta_{SO} = 3.4$ meV. By using a low Dirac field, we are able to identify a strong Zeeman-type coupling in two devices. The origin of the large magnitude of the spin-orbit splitting observed remains an open question. Nonetheless, the observed strength of the coupling is promising for many applications of the spin-orbit interaction in carbon nanotube devices.

Methods

Sample fabrication. The devices are made using a fabrication technique in which the nanotube is deposited in the last step of the fabrication. Single quantum dot devices were fabricated by growing the device across predefined structures with three gates, using W/Pt electrodes for electrical contacts to the nanotube, and a dry-etched doped silicon layer to make gates[23]. Double quantum dot devices were fabricated by growing the nanotube on a separate chip[33].

Measurements. Measurements were performed with a base electron temperature of 100 mK. For measurements performed with single quantum dot devices, a magnetic field was applied with an orientation in the plane of the sample, perpendicular to the trench. In measurements with double quantum dot devices, a 3D vector magnet was used to align the direction of the magnetic field along the axis of the nanotube. The measurement data sets presented in this manuscript are available online, see Supplemenatary Data 1.

Extraction of the ground state energies. In order to convert changes in gate voltage position of the Coulomb peak to changes in energy of the ground state, a scaling factor α is required that converts gate voltage shifts into an energy scale. This scaling factor is measured by the lever-arm factor from the Coulomb diamond data, such as that shown in Supplemenatary Fig. S3. In addition to the scaling of gate voltage to energy, the ground state magnetic field dependence traces must be offset by an appropriate amount, corresponding to subtracting the Coulomb energy from the addition energy, to produce spectra such as that shown in Fig. 3 of the main text. To determine this offset, we use the fact that at $B = 0$, time-reversal symmetry requires that the electron states are two-fold degenerate. The offset for the 1e/2e curves was thus chosen such that the extrapolated states are degenerate at $B = 0$. This was also used to determine the offset between the 3e/4e curves. For the remaining offset between the 2e and 3e curves, we use the level crossing that occurs at B_1. At B_1, the levels may exhibit a splitting due to intervalley scattering. This results in a ground state energy, which does not show a sharp kink at B_1, but instead becomes rounded. The rounding of this kink in our data, however, is small. We estimate $\Delta_{KK} \sim 0.1$ meV, and have offset the 2e/3e curves by this amount at the crossing at B_1. The spin-orbit splittings are determined by the zero-field gap in the resulting ground-state spectra. The error bars quoted on the spin-orbit splittings are estimates based on the accuracy with which the ground states energy curves can be aligned to produced plots such as those in Fig. 3 of the main text.

References

1. Kane, C. & Moore, J. Topological insulators. *Phys. World* **24,** 32–36 (2011).
2. Hasan, M. & Kane, C. Colloquium: topological insulators. *Rev. Mod. Phys.* **82,** 3045–3067 (2010).
3. Hsieh, D. *et al.* A topological Dirac insulator in a quantum spin hall phase. *Nature* **452,** 970–974 (2008).
4. Nowack, K., Koppens, F., Nazarov, Y. & Vandersypen, L. Coherent control of a single electron spin with electric fields. *Science* **318,** 1430–1433 (2007).
5. Nadj-Perge, S., Frolov, S., Bakkers, E. & Kouwenhoven, L. Spin-orbit qubit in a semiconductor nanowire. *Nature* **468,** 1084–1087 (2010).
6. Huertas-Hernando, D., Guinea, F. & Brataas, A. Spin-orbit coupling in curved graphene, fullerenes, nanotubes, and nanotube caps. *Phys. Rev. B* **74,** 155426 (2006).
7. Min, H. *et al.* Intrinsic and rashba spin-orbit interactions in graphene sheets. *Phys. Rev. B* **74,** 165310 (2006).
8. Kuemmeth, F., Ilani, S., Ralph, D. & McEuen, P. Coupling of spin and orbital motion of electrons in carbon nanotubes. *Nature* **452,** 448–452 (2008).
9. Churchill, H. *et al.* Relaxation and dephasing in a two-electron ^{13}C nanotube double quantum dot. *Phys. Rev. Lett.* **102,** 166802 (2009).
10. Jhang, S. *et al.* Spin-orbit interaction in chiral carbon nanotubes probed in pulsed magnetic fields. *Phys. Rev. B* **82,** 041404 (2010).
11. Jespersen, T. *et al.* Gate-dependent spin-orbit coupling in multielectron carbon nanotubes. *Nat. Phys.* **7,** 348–353 (2011).
12. Bulaev, D., Trauzettel, B. & Loss, D. Spin-orbit interaction and anomalous spin relaxation in carbon nanotube quantum dots. *Phys. Rev. B* **77,** 235301 (2008).
13. Flensberg, K. & Marcus, C. Bends in nanotubes allow electric spin control and coupling. *Phys. Rev. B* **81,** 195418 (2010).
14. Zazunov, A., Egger, R., Jonckheere, T. & Martin, T. Anomalous Josephson current through a spin-orbit coupled quantum dot. *Phys. Rev. Lett.* **103,** 147004 (2009).
15. Lim, J., López, R. & Aguado, R. Josephson current in carbon nanotubes with spin-orbit interaction. *Phys. Rev. Lett.* **107,** 196801 (2011).
16. Pályi, A., Struck, P., Rudner, M., Flensberg, K. & Burkard, G. Spin-orbit-induced strong coupling of a single spin to a nanomechanical resonator. *Phys. Rev. Lett.* **108,** 206811 (2012).
17. Ohm, C., Stampfer, C., Splettstoesser, J. & Wegewijs, M. Readout of carbon nanotube vibrations based on spin-phonon coupling. *Appl. Phys. Lett.* **100,** 143103 (2012).
18. Lutchyn, R., Sau, J. & Das Sarma, S. Majorana fermions and a topological phase transition in semiconductor-superconductor heterostructures. *Phys. Rev. Lett.* **105,** 077001 (2010).
19. Oreg, Y., Refael, G. & Von Oppen, F. Helical liquids and majorana bound states in quantum wires. *Phys. Rev. Lett.* **105,** 177002 (2010).
20. Klinovaja, J., Schmidt, M., Braunecker, B. & Loss, D. Helical modes in carbon nanotubes generated by strong electric fields. *Phys. Rev. Lett.* **106,** 156809 (2011).
21. Egger, R. & Flensberg, K. Emerging dirac and majorana fermions for carbon nanotubes with proximity-induced pairing and spiral magnetic field. *Phys. Rev. B* **85,** 235462 (2012).
22. Sau, J. & Tewari, S. Majorana fermions in carbon nanotubes. *Arxiv preprint arXiv: 1111.5622* (2011).
23. Steele, G., Gotz, G. & Kouwenhoven, L. Tunable few-electron double quantum dots and klein tunnelling in ultraclean carbon nanotubes. *Nat. Nano* **4,** 363–367 (2009).
24. Ando, T. Spin-orbit interaction in carbon nanotubes. *J. Phys. Soc. Jpn.* **69,** 1757–1763 (2000).
25. De Martino, A., Egger, R., Hallberg, K. & Balseiro, C. Spin-orbit coupling and electron spin resonance theory for carbon nanotubes. *Phys. Rev. Lett.* **88,** 206402 (2002).
26. Izumida, W., Sato, K. & Saito, R. Spin-orbit interaction in single wall carbon nanotubes: Symmetry adapted tight-binding calculation and effective model analysis. *J. Phys. Soc. Jpn.* **78,** 074707 (2009).
27. Jeong, J. & Lee, H. Curvature-enhanced spin-orbit coupling in a carbon nanotube. *Phys. Rev. B* **80,** 075409 (2009).
28. Klinovaja, J., Schmidt, M., Braunecker, B. & Loss, D. Carbon nanotubes in electric and magnetic fields. *Phys. Rev. B* **84,** 085452 (2011).
29. Deshpande, V. *et al.* Mott insulating state in ultraclean carbon nanotubes. *Science* **323,** 106–110 (2009).
30. Minot, E., Yaish, Y., Sazonova, V. & McEuen, P. Determination of electron orbital magnetic moments in carbon nanotubes. *Nature* **428,** 536–539 (2004).
31. Jarillo-Herrero, P. *et al.* Electronic transport spectroscopy of carbon nanotubes in a magnetic field. *Phys. Rev. Lett* **94,** 156802 (2005).
32. Jespersen, T. *et al.* Gate-dependent orbital magnetic moments in carbon nanotubes. *Phys. Rev. Lett.* **107,** 186802 (2011).
33. Pei, F., Laird, E., Steele, G. & Kouwenhoven, L. Valley-spin blockade and spin resonance in carbon nanotubes. *Nat. Nanotechnol.* **7,** 630–634 (2012).

Acknowledgements

We thank Daniel Loss, Jelena Klinovaja and Karsten Flensberg for helpful discussions. This work was supported by the Dutch Organization for Fundamental Research on Matter (FOM), the Netherlands Organization for Scientific Research (NWO), the EU FP7 STREP programme (QNEMS).

Author contributions

G.A.S., F.P., E.A.L., J.M.J. and H.B.M. performed the experiments; G.A.S., F.P. and H.B.M. fabricated the samples; G.A.S. wrote the manuscript; all authors discussed the results and contributed to the manuscript.

Additional information

Supplementary Information accompanies this paper at http://www.nature.com/naturecommunications

Competing financial interests: The authors declare no competing financial interests.

Reprints and permission information is available online at http://npg.nature.com/reprintsandpermissions/

How to cite this article: Steele, G.A. *et al.* Large spin-orbit coupling in carbon nanotubes. *Nat. Commun.* 4:1573 doi: 10.1038/ncomms2584 (2013).

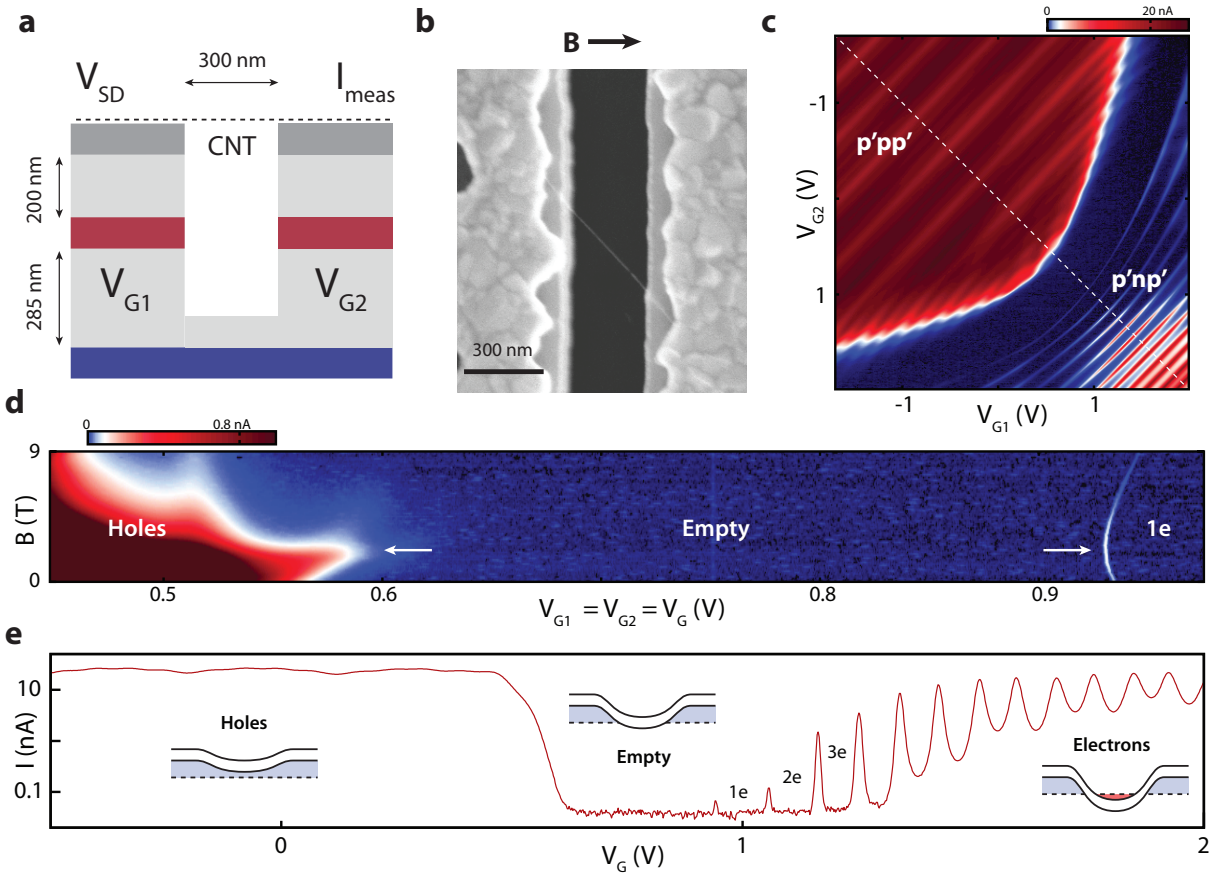

Supplementary Figure S1: Characterization of Device 1. a, Schematic of device 1, consisting of a clean nanotube grown over a predefined trench. Source and drain contacts to the nanotube are made by a 5/25 nm W/Pt bilayer (dark grey). Two gates embedded in the oxide (red) are used to induce charges in the nanotube. A backgate (blue) is kept grounded. **b,** A scanning electron microscope (SEM) image of the actual device, taken after all measurements. The nanotube axis lies at an angle of 48 degrees relative to the magnetic field orientation. **c,** I_{meas} at a $V_{sd} = 1$ mV as a function of the two gate voltages. **d,** Magnetic field dependence of I_{meas} along a diagonal line cut $V_{g1} = V_{g2} = V_g$ in **c**. The device exhibits a minimum gap at $B_{Dirac} = 2.2$ T (white arrows), corresponding to a crossing through the Dirac point of the graphene bandstructure by the $k_\perp$ quantization line. **e,** Plot of I_{meas} (logscale) at $V_{sd} = 1$ mV showing the gate voltages corresponding to the first electrons in the quantum dot.

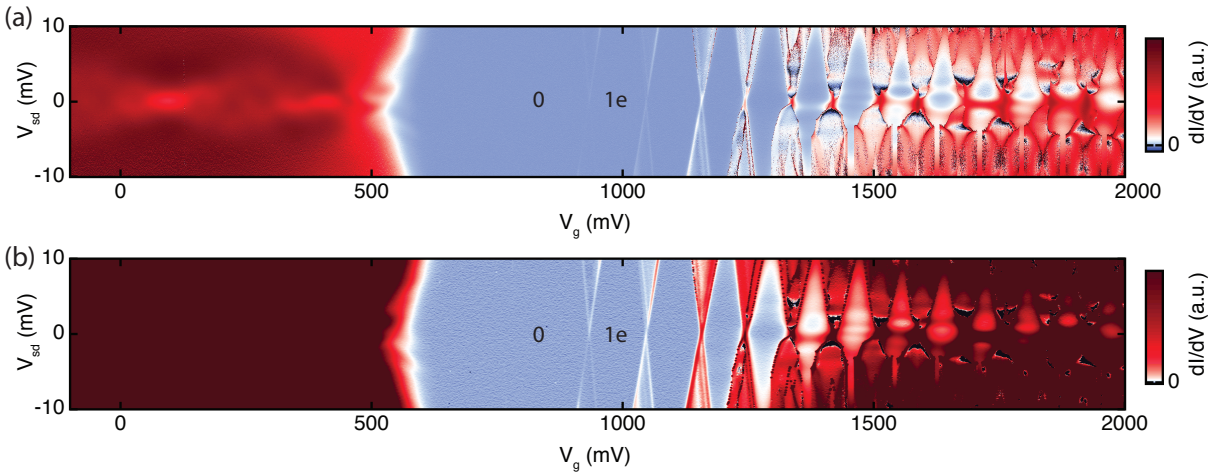

Supplementary Figure S2: Stability diagram showing Coulomb diamonds of Device 1. a, Differential conductance of device 1 showing the Coulomb diamonds of the first electrons, the empty device, and the threshold for hole conduction, taken at $B = 0$. For larger gate voltage, a four-fold pattern of Kondo resonances is observed, together with strong instabilities in the Coulomb diamonds which we attribute to mechanical excitation of mechanical resonances of the suspended nanotube by single-electron tunnelling [33]. Due to the lack of p-n junction barriers for holes, the hole doped region shows Fabry-Perot type oscillations. For the hole doped device, and for large electron numbers, we estimate the single-particle energy of the confined states to be ~ 5 meV. **b,** The same data as in **a** with the contrast enhanced in order to clearly show the Coulomb diamond of the first electron.

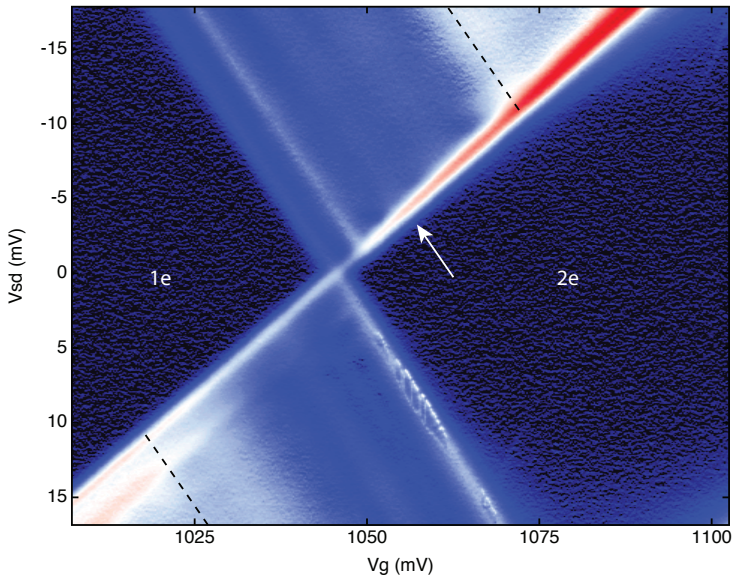

Supplementary Figure S3: Excited states of the 2e charge state in Device 1 Differential conductance vs. V_G and V_{SD} for the 1e to 2e transition, in which excited states could be resolved. The dashed lines indicates excited states we identify as the single-particle energy splitting ΔE_{SP}. For the 1e-2e transition, we extract $\Delta E_{SP} = 11$ meV. From $DeltaE = \hbar v_F/(2L)$, we estimate the size of the quantum dot $L \sim 200$ nm. From the measured angle in the SEM image, the total length of the nanotube over the trench is $\sim$ 400 nm. This implies a 100 nm length for the pn depletion region and p doped regions from the work function induced doping for the 1e quantum dot. For higher electron numbers, and similarly for holes, the single particle energy drops to 5 meV (see figure S4), implying a confinement length responding to the full length of the suspended nanotube. The white arrow indicates the position of a faint excited state with an energy ~ 3 meV, consistent with the spin-orbit splitting we observe from the ground state measurements.

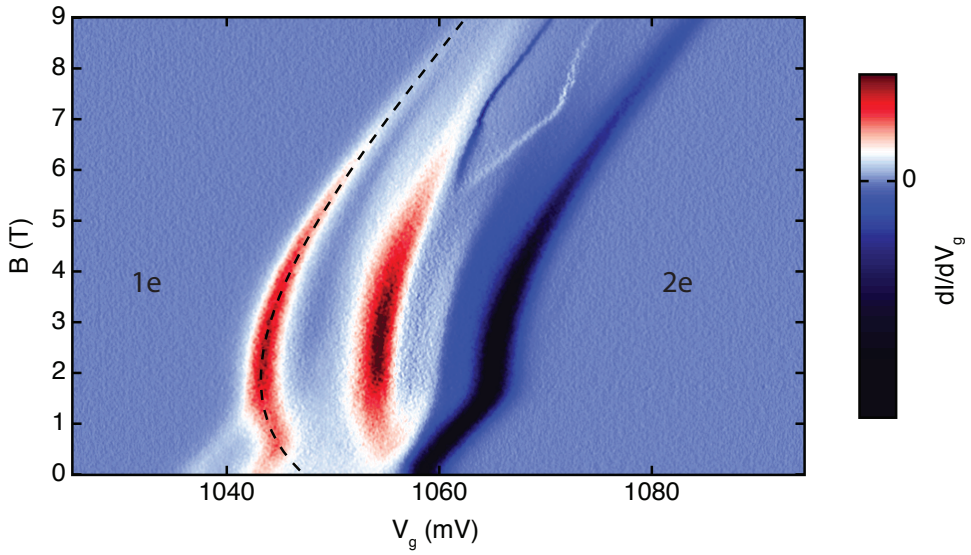

Supplementary Figure S4: Evidence for spin-orbit splitting in magnetic field spectroscopy of excited states in Device 1. A colourscale plot showing dI/dV_g as a function of magnetic field for the 1e/2e transition of device 1 taken at $V_{SD} = 5.5$ mV. Excited states of the 2e ground state appear as positive peaks in dI/dV_g. The dashed line indicates the magnetic field dependence of a 2e excited state consistent with the expected spectrum from spin-orbit splitting. From the excited state data, we extra a spin-orbit splitting $\Delta_{SO} = 2.9$ meV, lower than that from the ground state measurements. This difference can arise from a difference between the excited state energies of the 2e state compared to the ground state energy of 3e from electron interactions. The origin of the extra excited state running parallel to the ground state for fields less than B_1 is not understood. The value of Δ_{SO} from the excited state measurement is, similar to that from the ground state measurements, an magnitude larger than the expected maximum $\Delta_{SO}^{max} = 106$ μeV expected from theory (see table S1). Excited states in the 0/1e transition did not show clear visibility, and those of higher states were masked by instabilities we attribute to mechanical excitation of the suspended nanotube (also visible here above 6T).

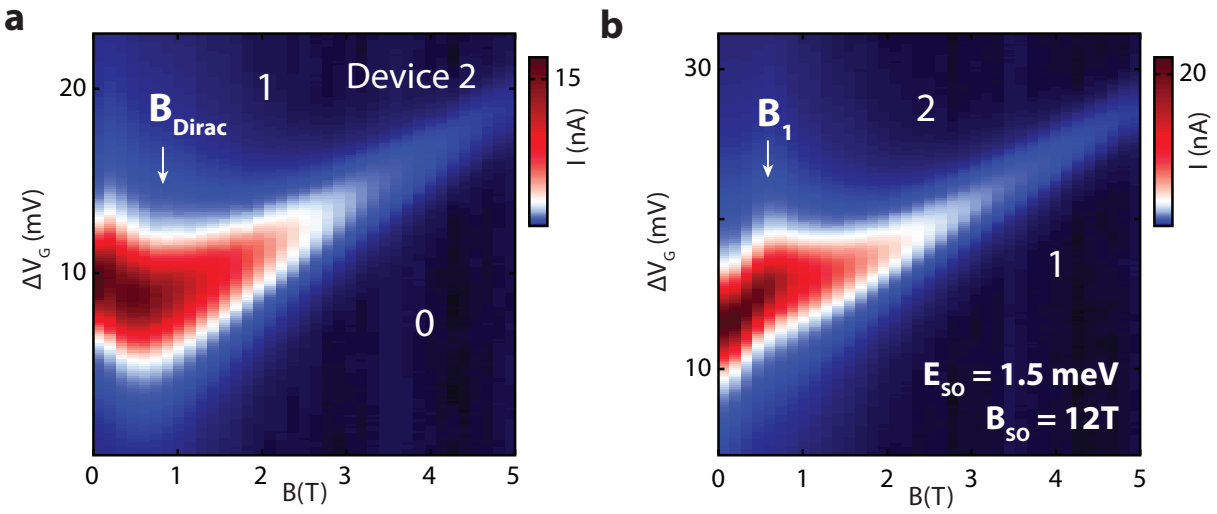

Supplementary Figure S5: Spin-orbit split states in Device 2. Magnetic field dependence of the first two electrons in device 2, showing the signature of the nanotube spin-orbit coupling with $\Delta_{SO} = 1.5$ meV.

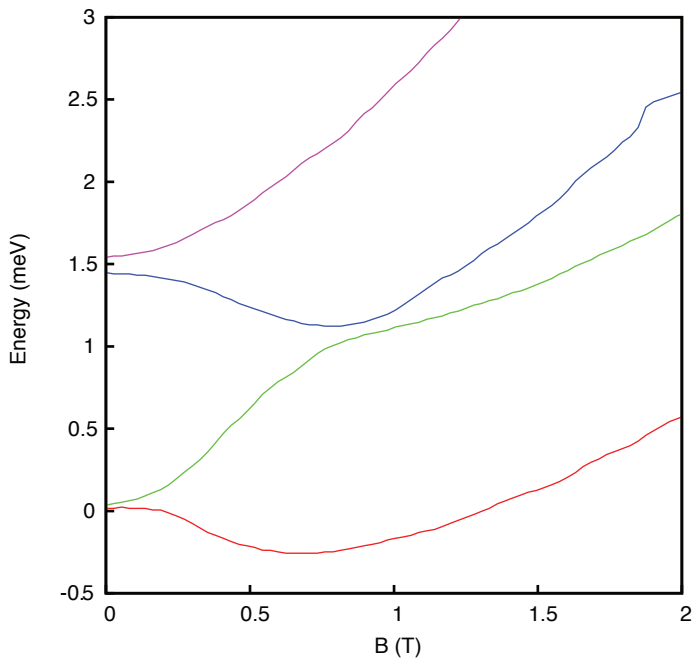

Supplementary Figure S6: Spin-orbit spectrum of the first shell in Device 2. Extracted ground state energies of the first four electrons in device 2. Device 2 also shows a large spin orbit coupling with a dominant Zeeman-type contribution. Note that the flat behaviour of the ground states at zero magnetic field is a measurement artifact from the magnetic field controller, see text for discussion.

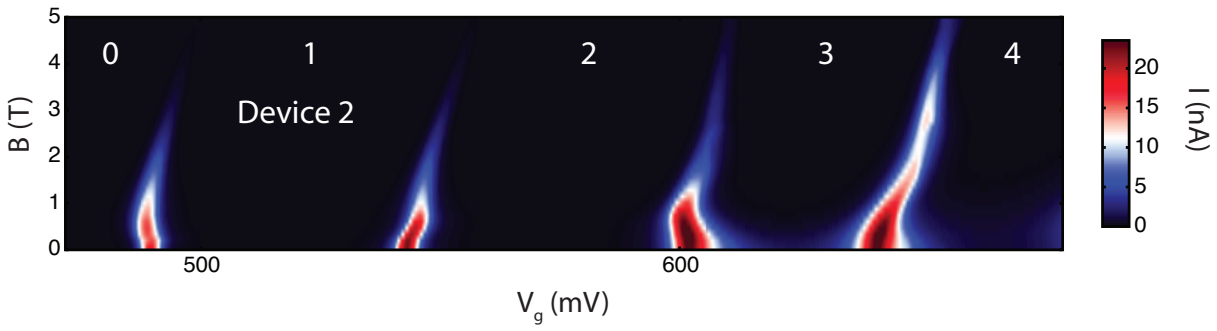

Supplementary Figure S7: Magnetic field dependence of the first four Coulomb peaks in Device 2. Coulomb blockade current vs. magnetic field and gate voltage for device 2, used to extract the ground state energies of the first shell, $V_{sd} = 1$ mV. The data in figure S6 is a zoom of the data here.

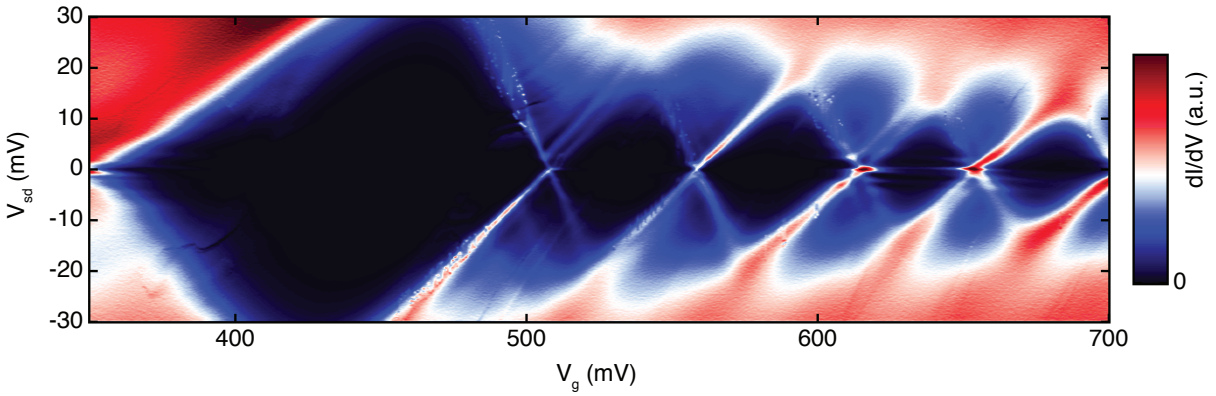

Supplementary Figure S8: Stability diagram of Device 2 in few-electron regime. a, Differential conductance of device 2 showing the Coulomb diamonds of the first electrons, the empty device, and the threshold for hole conduction, taken at $B = 0$.

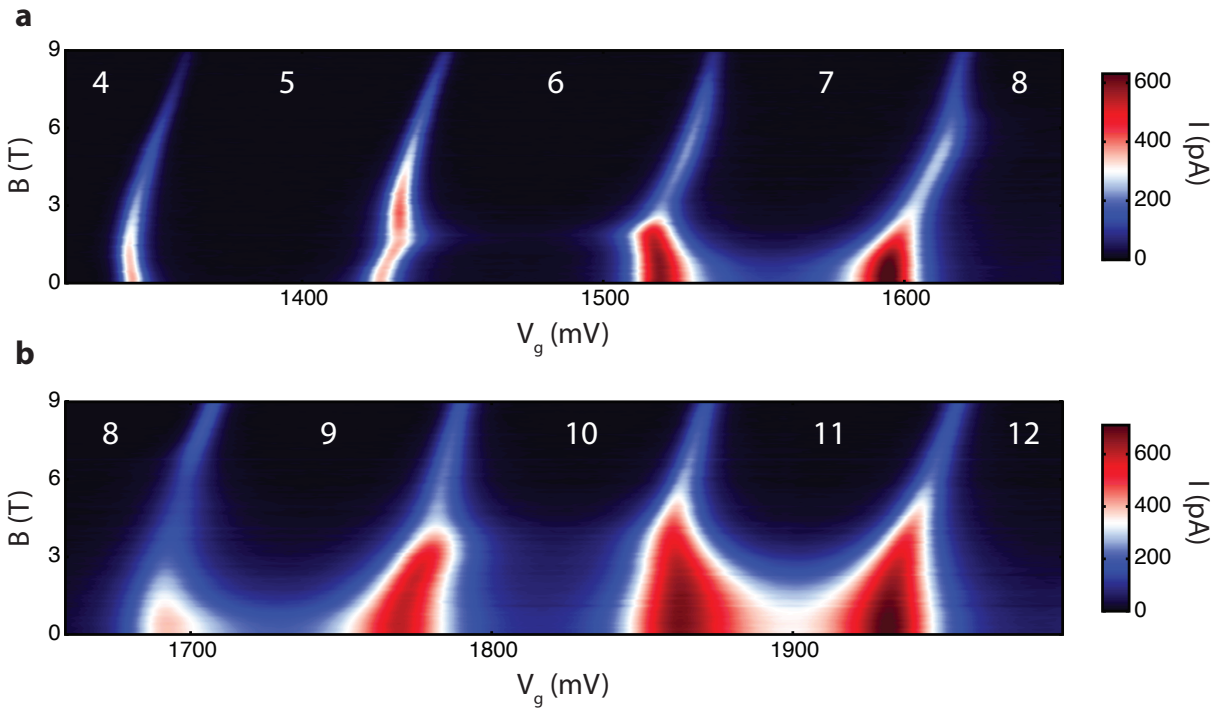

Supplementary Figure S9: Coulomb peak data for Shells 2 and 3 of Device 1. Measurements of I_{meas} vs. Vg and B on device 1 that are used to extract the energy spectra shown in figure 3 of the main text, taken at $V_{sd} = 70$ μV.

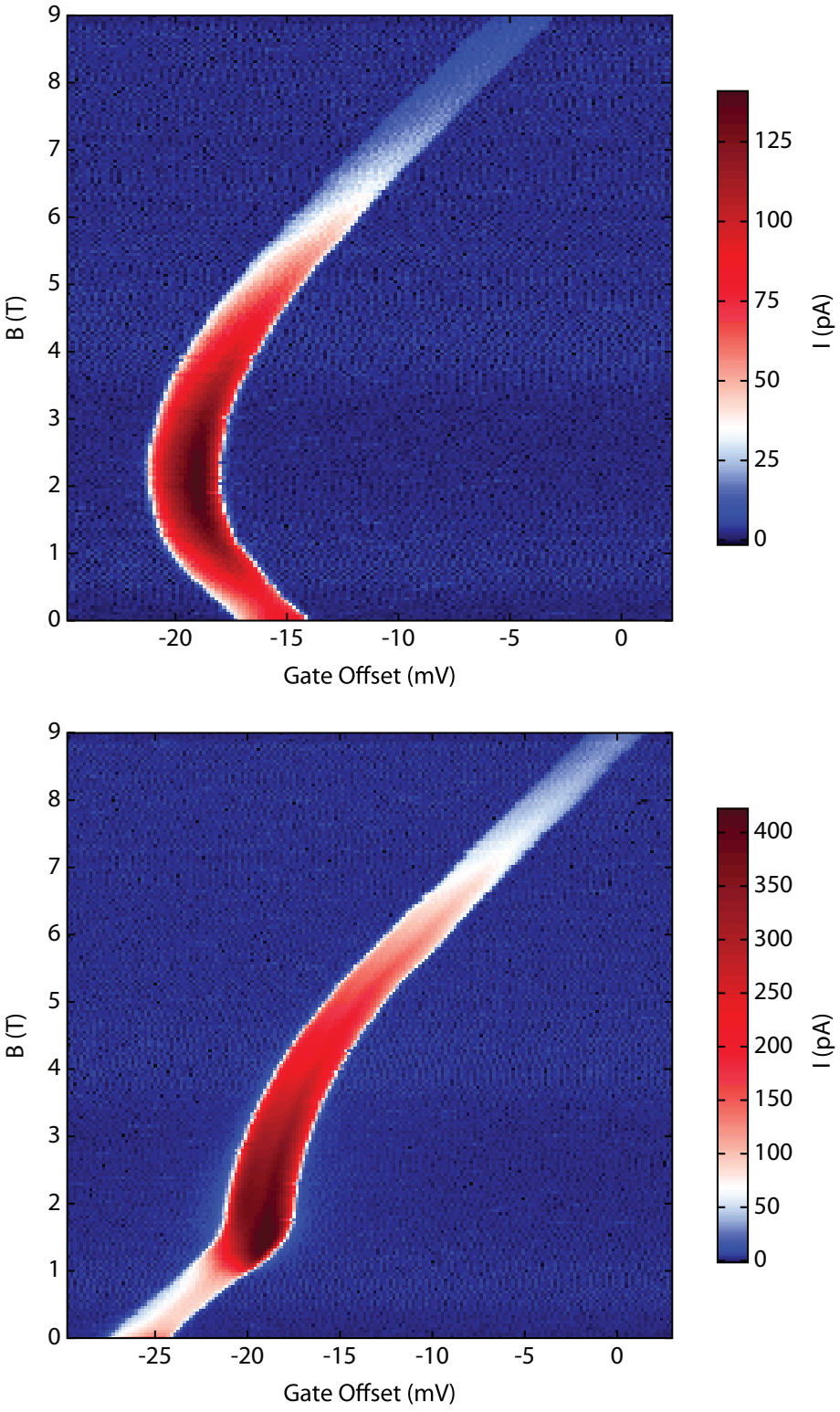

Supplementary Figure S10: High resolution datasets in Device 1 of spin-orbit states. High resolution datasets of the 1e and 2e Coulomb peaks of device 1 with $V_{SD} = 1$ mV, showing behaviour at low magnetic fields. Here, the low field behaviour is not affected by artifacts in the first gate sweep first gate sweep at because of a slow sweep rate of the gate that provided sufficient time for the magnetic field controller to settle before reaching the position of the Coulomb peak.

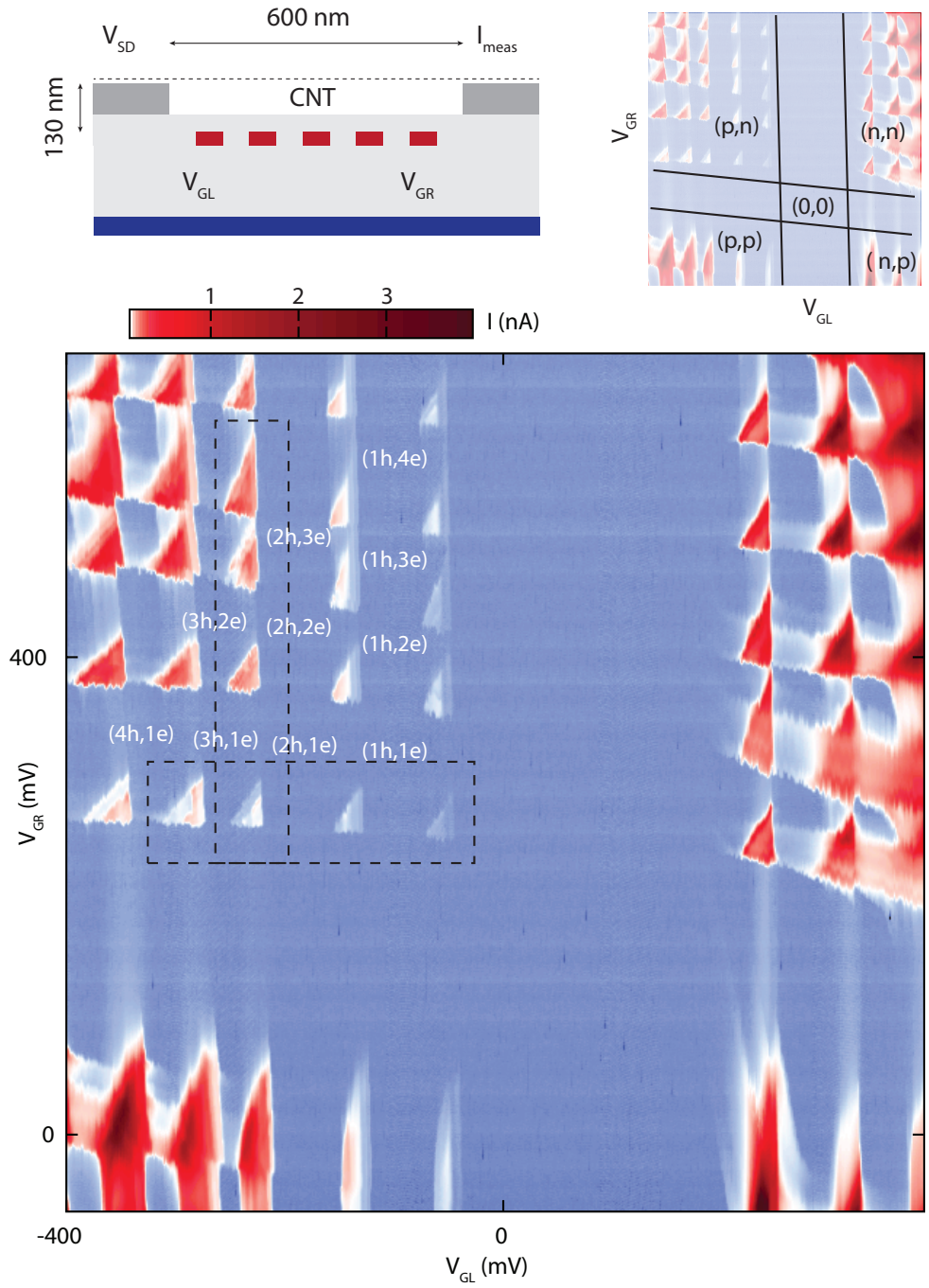

Supplementary Figure S11: Characterization of Device 3. a, Schematic of device 3. The total device length is 600 nm. The device includes 5 local gates embedded in oxide under the suspended nanotube. In the measurements, the outermost gates (V_{GL}, V_{GR}) are used to tune the electron/hole number in a (p,n) type double quantum dot, while the inner three gates are used to tune the interdot tunnel barrier. **b,** An overview of gate space, indicating the (p,p), (p,n), (n,p), and (n,n) regions of gate space, and the identification of the (0,0) configuration. **c,** A color scale plot of the measured current as a function of V_{GL} and V_{GR} at $V_{SD} = 10$ mV. The boxes outlined by dashed lines show the triple points used to track the ground state energies in figure S12 and figure 4 of the main text.

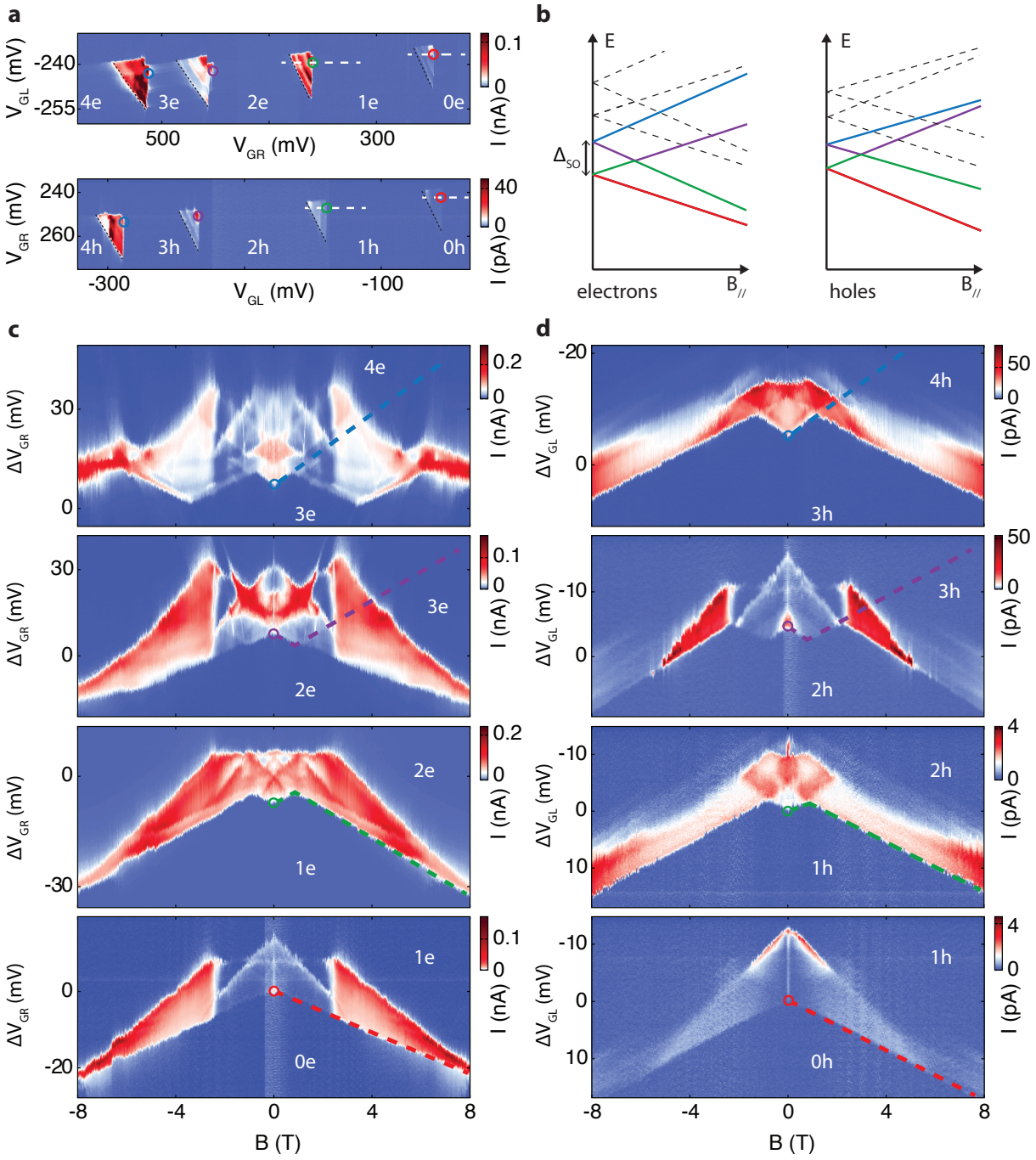

Supplementary Figure S12: Energy spectra of the first electron shell and hole shell of Device 3. Extended datasets from figure 4 of the main text, showing the ground states of the first four electrons and the first four holes, extracted from the motion of the triple points indicated in the dashed boxes in figure S11 with magnetic field. **a,** Double-dot stability diagrams taken at $V_{sd} = 5$ mV. **b,** Expected spectra for the first four electrons (solid lines), as well as spectra from the next higher shell (dashed lines). **c,d,** Magnetic field dependence of gate space cuts (white dashed lines in **a**) for the first four electrons **c** and holes **d**. Similar to previous works [8], the magnetic field dependence of the third and fourth electrons/holes does not follow exactly the single-shell spin orbit spectrum (solid lines in **b**), but instead show extra crossings from downward moving levels in higher shells (dashed lines in **b**).

Supplementary Table S1: Summary of previous spin-orbit measurements.

Reference	μ_{orb}	$d^{\star}$	Δ_{SO}^{max} theory	Δ_{SO} observed
Kuemmeth *et al.* [8]	1.55 meV/T	7.0 nm	110 μeV	370 μeV (1e) 210 μeV (1h)
Jespersen *et al.* [8]	0.63 meV/T	2.9 nm	168 μeV	150 μeV (many electrons)
Jespersen *et al.* [31]	0.87 meV/T	5.3 nm†	146 μeV	200 μeV (many electrons)
Churchill *et al.* [9]	0.33 meV/T	1.5 nm	520 μeV	170 μeV (1e)
Jhang *et al.* [10]	0.33 meV/T$^{\diamond}$	1.5 nm**	520 μeV	2500 μeV††
Device 1	1.6 meV/T	7.2 nm	106 μeV	3400 μeV (1e)
Device 1	1.6 meV/T	3 nm‡	260 μeV	3400 μeV (1e)
Device 2	1.5 meV/T	6.8 nm	116 μeV	1500 μeV (1e)
Device 3	0.9 meV/T	4.1 nm	190 μeV	1700 μeV (1e)
Device 3	0.8 meV/T	3.7 nm	208 μeV	1300 μeV (1h)

* Estimated from the observed orbital magnetic moment, ignoring effects of $k_{||}$, unless otherwise noted

† The value of the diameter for this entry is based on a detailed analysis of μ_{orb} as a function of shell number performed by the authors.

‡ The diameter for this entry is based on the observed AFM height of the nanotube.

$^{\diamond}$ Orbital moment implied from AFM diameter.

** Diameter from AFM.

†† Implied from bulk bandgap measurements.

Supplementary Note 1: Characterization of Device 1

A schematic of Device 1 is shown in figure S1**a**. Similar to previous studies[22], we make a clean suspended carbon nanotube quantum dot by growing the nanotube across a pre-defined structure in the last step of the fabrication. A SEM image of the actual device (taken after all measurements were completed) is shown in figure S1**b**. As we do not control the direction of the nanotube growth, it often crosses the trench at an angle, as can be seen in this device. From AFM measurements, we estimate the nanotube diameter to be 3 nm.

We apply a d.c. voltage across the source and drain of the device and measure the current through the nanotube as we sweep the gates, as shown in figure S1**c**. In the upper left corner of the plot, the gates dope the center of the nanotube with holes. Near the edge of the device, the gate electric fields are screened by the ohmic contact metal; here, the doping is set by the work function difference between the metal ($\Phi_{Pt} \sim 5.6$ eV) and the nanotube ($\Phi_{CNT} \sim 4.9$ eV), resulting in a gate-independent hole doping at the edge of the trench. This, combined with hole doping of the suspended segment from the gates, results in a p′pp′ configuration in the upper left corner of figure S1**c**. In this region, we observe only weak modulations of the conductance which does not vanish between peaks, indicating a highly transparent interface between the Pt metal and clean nanotube. In the lower right corner of figure S1**c**, the gates induce electrons in the suspended segment, giving a p′np′ doping profile. Electrons occupy a quantum dot with tunnel barriers defined by p-n junctions [22], in which we can count the number of carriers starting from zero, shown in figure S1**e**.

Figure S1**d** shows I_{meas} vs. V_g taken along the dotted line in S1**c** as a function of an external magnetic field applied in the plane of the sample, perpendicular to the trench. The distance in gate voltage between the onset of electron and hole current is a measure of the electronic bandgap of the nanotube. In carbon nanotubes, a magnetic field component parallel to the nanotube axis shifts the quantization condition of the states circling the circumference ($k_\perp$) by an Arahonov-Bohm flux, and therefore reduces the nanotube bandgap (see figure 2**a** of main text). For sufficiently large magnetic fields, the $k_\perp$ quantization line will cross the Dirac point of the graphene bandstructure and the bandgap begins to increase again. In our device, this occurs at a magnetic field of $B_{Dirac} = 2.2$ T, indicated by white arrows in figure S1**d**. This implies a contribution to the electronic bandgap $E_{gap}^{k\perp} = 2\hbar v_F \Delta k_\perp \sim 7$ meV arising from the shift of the $k_\perp$ quantization line. In this sense, our nanotube is very close to the metallic condition in which the $k_\perp$ quantization line passes directly through the center of the Dirac cone. This is a very different regime compared to previous devices where the nanotube spin orbit coupling was studied [8,11], in which no such evidence of a low Dirac field was seen. Similar to previous studies where low Dirac fields were reported [28], the bandgap do not vanish at the Dirac point. We observe a residual gap in the transport data at the Dirac point of about 80 meV, measured by subtracting the average of the addition energies from the first electron and the first hole from the addition energy of the empty quantum dot.

Supplementary Note 2: Spin orbit splitting in Device 2

In figures S6-S9, we present the magnetic field dependence of the ground states of the first four electrons in a second nearly metallic carbon nanotube (device 2). Device 2 is similar in design to device 1, but includes only a backgate. The trench length is 800 nm. In device 2, we observe a Dirac field of 0.8 T, an orbital magnetic moment $\mu_{orb} = 1.5$ meV/T, and a spin orbit splitting $\Delta_{SO} = 1.5$ meV.

Supplementary Note 3: Model for a nearly metallic nanotube with spin-orbit coupling

In order to calculate the spectra plotted in figures 2**g** and **h** of the main text, we use a model of the nanotube based on the graphene bandstructure with a parallel magnetic field. In a basis of spin and valley eigenstates in which the spin direction is defined parallel to the axis of the nanotube, the Hamiltonian consists of a 4x4 matrix with only diagonal elements given by:

$$E(v,s,B) = \sqrt{(E_{k\perp} + vs\Delta_{SO}^{orb} + v\mu_{orb}B)^2 + E_{k\|}^2} + vs\Delta_{SO}^{Zeeman} + \frac{1}{2}sg\mu_B B \tag{S1}$$

Here, v and s take on values ± 1 depending on the electron spin and the valley it occupies, $E_{k(\|,\perp)} = \hbar v_F k_{(\|,\perp)}$ where $k_{(\|,\perp)}$ are the momentum of the electron relative to the Dirac points in the directions parallel and perpendicular to the axis of the nanotube, and Δ_{SO}^{orb} and Δ_{SO}^{Zeeman} are the orbital and Zeeman type spin orbit splittings at $k_{||} = 0$ (α and β). These diagonal elements correspond to the energies plotted in figure 3. In the calculations, we have chosen to make the total spin orbit coupling either purely orbital or purely Zeeman for illustrative purposes, and have used the following parameters: $\Delta_{SO} = 2$ meV, $E_{k\|} = 1$ meV, $E_{k\perp} = 2$ meV, and $\mu_{orb} = 0.9$ meV/T.

Including the observed 48 degree misalignment of the magnetic field to the nanotube axis, the Zeeman splitting Hamiltonian $g\mu_B \vec{B} \cdot \vec{S}$ is no longer diagonal in this basis, and the eigenstates are mixtures of the four basis states described above. However, because the Bohr magneton is small compared to the orbital magnetic moment, this effect is weak and does not result in qualitative different spectra.

The Zeeman-type contribution to the spin-orbit splitting, according to current theoretical estimates, is expected to be larger than the orbital-type contribution by as much as a factor of 4, except for in nanotube chiralities where it vanishes or is small due to the $\cos(3\theta)$ term ($\theta = 0$ corresponding to a zigzag nanotube). It is an open question, however, why the spin-orbit splitting we observe in devices 1 and 2 is so dominantly of the Zeeman-type, with little indication of an orbital contribution.

Supplementary Note 4: Discussion of summary table of previous spin-orbit spliting measurements

In Supplementary Table S1, we summarize in a table our measurements together with other measurements of the spin-orbit coupling reported in literature. As described in the main text, we use the formula for the nanotube spin-orbit splitting from [27], given by:

$$H_{SO}^{cv} = \alpha S^z \sigma_1 + \tau \beta S^z \tag{S2}$$

with the orbital contribution given by:

$$\Delta_{SO}^{orb} = \alpha = \frac{-0.08 \text{ meV nm}}{r} \tag{S3}$$

and the Zeeman contribution given by:

$$\Delta_{SO}^{Zeeman} = \beta = \frac{-0.31 \text{ meV nm}}{r} \tag{S4}$$

where r is the radius of the nanotube. For the maximum theoretical value, we choose $\theta = 0$, giving:

$$\Delta_{SO}^{max} = \frac{780 \ \mu\text{eV}}{d \text{ (in nm)}} \tag{S5}$$

In order to provide a consistent comparison, we have estimated the (minimum) diameter using the observed value of the orbital magnetic moment μ_{orb}. Assuming a Fermi velocity of 0.9×10^6 m/s, μ_{orb} is given by:

$$\mu_{orb} = \frac{dev_F}{4} = 220 \ \mu\text{eV / T} \times d \text{ (in nm)} \tag{S6}$$

where v_F is the Fermi velocity of the graphene bandstructure, which we take here as 0.9×10^6 m/s. Here, we assume $v_{F\perp} = v_F$, and therefore have not accounted for the reduction of μ_{orb} from a finite $k_{||}$ [31]. The resulting estimates of d from μ_{orb} represent a lower bound on the diameter (and thus also an upper bound on Δ_{SO}^{max}).

We have also included three entries in which we calculate Δ_{SO}^{max} based on a different estimate of the diameter. These three entries correspond to the diameter $d = 3$ nm we estimate from AFM measurements on device 1, the diameter $d = 5.3$ nm estimated by [31] from an extensive analysis of μ_{orb} as a function of gate voltage, and the diameter $d = 1.5$ nm measured by Jhang *et al.* [10]. Note that the tapping-mode AFM measurement of the diameter may underestimate the diameter of single-wall carbon nanotubes due to compression forces from the AFM tip.

The measurements referred to in the table were performed by tracking the electronic states of indi-

vidual levels in a quantum dot at low temperatures, except for the measurements of Jhang *et al.* [10]. The values in [10] are based on measurements of the nanotube bandgap implied from device conductance near the bandgap as a function of magnetic field at different fixed gate voltages, together with the nanotube diameter as measured by AFM. The devices measured here and those measured by Kuemmeth *et al.* [8] were made using clean nanotubes grown in the last step of the fabrication, while the other measurements were performed on nanotubes which were grown first and subsequently underwent processing in the cleanroom.

Finally, we also note that when using μ_{orb} to estimate the nanotube diameter, we obtain a number that is not only larger than the AFM measurement for device 1, but also larger than the largest diameter expected for single wall carbon nanotubes in, for example, transmission electron microscope studies. This is also the case for many of the devices in Table 1. Such a discrepancy was also noted by earlier authors [31], and remains unresolved. One suggestion of the authors of [31] was a renormalization of the Fermi velocity. Such a renormalization could arise from, for example, discrepancies between the experimental tight binding parameters of carbon nanotubes and those obtained from *ab initio* calculations.

Supplementary Note 5: Artifacts in extracted ground state energies at $B < 0.15$ T

Note that there is glitch in the first line of the data set in figure S6. This artifact is also present to a lesser degree figures 1(c)-(f) and the resulting extracted energies in figures 3(a)-(c) of the main text. This glitch results in an artifact in the resulting extracted ground state energies plotted in figure S5 in the form of a flat slope for $B < 150$ mT. The glitch and resulting artifacts arise from the inability of our magnetic controller to track the setpoint field during faster magnetic field sweeps. The effects of these artifacts are limited to the first gates sweep (row) of the Coulomb peak magnetic field dependence data. These artifacts have been accounted for in the estimation of the error bar on Δ_{SO}.

In order to demonstrate that these artifacts are not obscuring possible other phenomena at very low magnetic fields, we have also included high resolution datasets in figure S10 for the data in figure 1(c) and 1(d) of the main text. Here, the gate was swept sufficiently slowly that the magnet controller had time to settle before the gate voltage reached the position of the first Coulomb peak, and thus the artifacts are not present.

Supplmentary Note 6: Device 3 characterization and analysis

In this section, we present a basic characterization of device 3 (figure S11), together with measurements the magnetic field dependence of the ground state energies of the first four electrons and first four holes in the device (figure S12), and discuss the extraction of the ground state energies from the magnetic field dependence of the gate-space cuts through the triple-point triangles.

By tracking the gate voltage position of any fixed point on the triple-point bias triangles as a function of magnetic field, we can independently track the ground state energy of the left and right dot in the double quantum dot device. This is analogous to the tracking of the ground states of a single quantum dot by following the Coulomb peak position with magnetic field. To make this concrete, we illustrate this in the context of upper left bias triangle in figure 4**a** of the main text, corresponding to the (3h,1e) $\leftrightarrow$ (2h,0e) transition. In the case that there is very small crosstalk capacitance from the left gate to the right dot (as is the case in figure 4**a** of the main text where the edges of the triple-point bias triangle are nearly vertical), vertical shifts of the bias triangle arise from shifts in the 3h ground state, while shifts in the 1e ground state shift the bias triangle horizontally. In measuring the shift of the bias triangle, it is equivalent to track any fixed point on the triangle. We choose to extract the ground state energies by following a point near the tip of the triangle, as the current on the baseline in our device is weak due to weakly tunnel-coupled ground states.

Supplementary References

[34] Steele, G. *et al.* Strong coupling between single-electron tunneling and nanomechanical motion. *Science* **325**, 1103 (2009).